Organic & Biomolecular Chemistry

PAPER

View Article Online
View Journal | View Issue

Cite this: *Org. Biomol. Chem.*, 2017, **15**, 8827

Exploring the origins of selectivity in soluble epoxide hydrolase from *Bacillus megaterium*†

Eila Serrano-Hervás, [a] Marc Garcia-Borràs *[b] and Sílvia Osuna *[a]

Received 26th July 2017,
Accepted 5th October 2017

DOI: 10.1039/c7ob01847a

rsc.li/obc

Epoxide hydrolase (EH) enzymes catalyze the hydration of racemic epoxides to yield their corresponding vicinal diols. These enzymes present different enantio- and regioselectivity depending upon either the substrate structure or the substitution pattern of the epoxide ring. In this study, we computationally investigate the *Bacillus megaterium* epoxide hydrolase (BmEH)-mediated hydrolysis of racemic styrene oxide (*rac*-SO) and its *para*-nitro styrene oxide (*rac*-*p*-NSO) derivative using density functional theory (DFT) and an active site cluster model consisting of 195 and 197 atoms, respectively. Full reaction mechanisms for epoxide ring opening were evaluated considering the attack at both oxirane carbons and considering two possible orientations of the substrate at the BmEH active site. Our results indicate that for both SO and *p*-NSO substrates the BmEH enantio- and regioselectivity is opposite to the inherent (*R*)-BmEH selectivity, the attack at the benzylic position (C1) of the (*S*)-enantiomer being the most favoured chemical outcome.

1. Introduction

Enantiomerically pure compounds are commonly identified as key synthons for the manufacturing of bioactive products in the pharmaceutical and agrochemical industries. Both epoxide-containing substrates and their corresponding 1,2-diol products are essential chiral building blocks of pharmaceuticals.[1–5] For instance, aryl glycidyl and naphthyl ethers are potentially useful compounds for the production of chiral amino alcohols such as (*S*)-alprenolol and (*S*)-propranolol β-blocker drugs.[6]

The resolution of epoxide racemic mixtures is an attractive synthetic strategy for obtaining optically pure bioactive compounds of pharmacological interest. To this end, many different strategies are available that include the use of metal or organo-based catalysts,[7] but also biocatalysts such as monooxygenases.[8] However, these (bio)chemical approaches are not very efficient, and usually offer moderate yields of pure enantio-enriched epoxides, thereby making them less useful for organic synthesis.[9] In pursuit of more efficient methodologies, the use of epoxide hydrolases (EHs) has emerged as a potential synthetic route due to some of the EH key properties such as: (i) it is a cofactor independent enzyme; (ii) it is found in a huge number of organisms; (iii) it is capable of operating in organic solvents; and (iv) it can exhibit high enantio- and regioselectivity.[10,11] In particular, *Bacillus megaterium* ECU1001 epoxide hydrolase (BmEH) has an inherently high (*R*) enantioselectivity towards phenyl glycidyl ethers (PGE, see Scheme 1),[12–14] for which some other EHs have only shown modest enantioselectivity or are (*S*)-specific.[15–17] The BmEH enzyme also exhibits an excellent enantiomeric ratio ($E > 200$) towards a *para*-nitro styrene oxide (*p*-NSO) compound.[12] For the latter case, it was found that the nature of the *para*-substituent switches both BmEH enantio- and regioselectivity, with the hydrolysis of the (*S*)-enantiomer *via* the attack at the benzylic position being favoured (see Scheme 1).[12,18]

The BmEH enzyme belongs to the α,β-hydrolase fold, consisting of a three-dimensional (3D) structure that possesses an α,β sheet core domain and a lid domain that caps the active site.[19–21] The EH members of this α,β-hydrolase superfamily

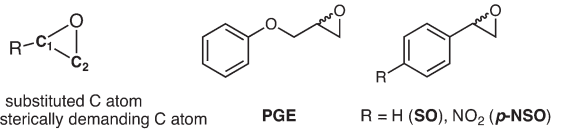

C_1: most substituted C atom
C_2: less-sterically demanding C atom

PGE

Scheme 1 Left, general representation of epoxide (carbon atoms labelled). Right, phenyl glycidyl ether (PGE) and the substrates used in this study: styrene oxide (SO), and *p*-nitro styrene oxide (*p*-NSO).

[a]*Institut de Química Computacional i Catàlisi (IQCC) and Departament de Química, Universitat de Girona, Carrer Maria Aurèlia Capmany 69, 17003 Girona, Spain. E-mail: silvia.osuna@udg.edu*

[b]*Department of Chemistry and Biochemistry, University of California, Los Angeles, 607 Charles E. Young Drive East, Los Angeles, CA 90095, USA. E-mail: marcgbq@gmail.com*

†Electronic supplementary information (ESI) available. See DOI: 10.1039/c7ob01847a

are characterised for having a highly conserved catalytic triad (Asp–His–Asp/Glu), two tyrosine residues positioned on the lid domain responsible for substrate recognition and for assisting the epoxide ring opening, and a conserved oxyanion motif consisting of HGXP residues (X = F in BmEH, see Fig. 1).[20,22,23]

EHs catalyse the addition of a water molecule to racemic epoxide-containing substrates to yield optically active 1,2-diols *via* biocatalytic hydrolytic kinetic resolution (HKR) and enantioconvergent hydrolysis of epoxides.[24–28] The mechanism by which these enzymes operate has long been debated.[29–33] However, it is generally accepted that EHs from the α,β-hydrolase fold share a common mechanism that takes place *via* a two-step mechanism through the formation of alkyl-enzyme intermediates (see Scheme 2, with BmEH labelling).[34–36] Upon initial binding of the epoxide substrate with Tyr144 and Tyr203 (see Fig. 2), the first step involves the nucleophilic attack by the Asp97 side chain at one of the epoxide carbons to generate a covalently bound alkyl-enzyme intermediate (**Int1** in Scheme 2). In the second step of the proposed mechanism, His267 acts as a general base to facilitate the nucleophilic activation of a water molecule to attack the Asp97 carbonyl, generating a new tetrahedral intermediate hereafter called **Int2**. The negatively charged tetrahedral intermediate is stabilized through hydrogen bond interactions between the backbone amide groups of the oxyanion hole residues Gly29–Phe30 and Asp97–Trp98. In the final step, the tetrahedral intermediate rearranges and dissociates to yield the corresponding 1,2-diol product (**Prod** in Scheme 2).

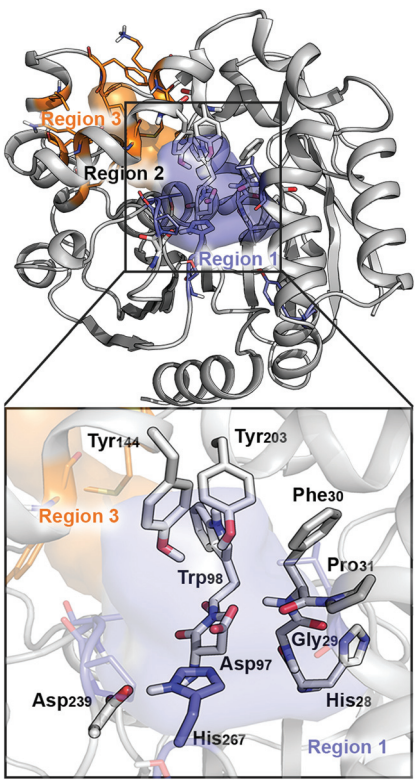

Fig. 1 Representation of the active site (region 2) of the BmEH enzyme (PDB: 4NZZ). The most important residues for the reaction are represented in sticks, and non-polar hydrogens are omitted for clarity. The BmEH region 1 (substrate entrance) and region 3 (product release) surfaces are highlighted in blue and orange, respectively. The two possible binding modes are also indicated as "region 1", *i.e.* substrate substituent pointing towards His267, and "region 3", substituent pointing towards Trp98.

Different computational approaches[37] have been used to explore the overall mechanism and selectivity of soluble EHs (sEHs). Truncated *theozyme* and cluster model calculations have been successfully applied to study the role and impact of enzyme active site residues in catalysed epoxide ring opening reaction mechanisms and selectivities.[38,39] Hopmann and Himo applied the cluster model (CM) approach on the X-ray structure of human soluble EH (sEH) to explore the role of the two conserved catalytic tyrosine residues.[23] Their results showed that one Tyr is enough for the alkylation reaction to occur, although the barrier increases by *ca.* 6.7 kcal mol^{-1} as compared to the wild-type. A drastic change in the activation barriers was observed for the double tyrosine mutant (*i.e.* larger barriers of *ca.* 24.8 kcal mol^{-1} were found after mutating both Tyr to Phe) indicating that this enzyme variant must be inactive. These results demonstrate that the presence of H-bond donors to activate the epoxide ring and stabilize the negative charge developed during the course of the reaction is essential.[40]

Amrein *et al.* carried out empirical valence bond (EVB) simulations of the enantio- and regioselective hydrolysis of *trans*-stilbene oxide (TSO) catalysed by *Solanum tuberosum* epoxide hydrolase I (StEH1).[30] EVB calculations suggested that the alkylation step for (*S*,*S*)-TSO at the benzylic C1 position is preferred by 1.7 kcal mol^{-1}, whereas the attack at the terminal C2 is favoured by 3.6 kcal mol^{-1} for (*R*,*R*)-TSO. However, high-energy barriers were found for both enantiomers for the hydrolysis step of the alkyl-enzyme intermediate that is formed after the Asp nucleophilic attack at C1 (**Int1** in Scheme 2). Therefore, the regioselectivity of the asymmetric epoxide ring opening of TSO by StEH1 is determined in the hydrolysis step, only the trajectories following the Asp attack at C2 for both enantiomers being productive. They also highlighted the relevance of considering a second active site histidine residue doubly protonated to properly describe the system. This histidine, which interacts with the nucleophilic aspartate, was thought to balance the negative charge developed during the catalysis.

In a very recent study, Lind and Himo applied the CM approach to explore the enantioconvergent resolution of racemic styrene oxide (SO) by using StEH1.[41] To investigate the origins of StEH1 selectivity, a very large CM system (of 279 atoms) was designed based on the StEH1 X-ray crystal in complex with the competitive inhibitor valpromide (PDB: 2CJP). The authors investigated the reaction mechanism considering both enantiomers, and examined the two possible binding modes of each enantiomer considering both the shape of the active site pocket and the substitution pattern of the substrate. Their results showed that (*S*)-SO is preferably attacked at C1 by the catalytic Asp, whereas for the (*R*)-SO

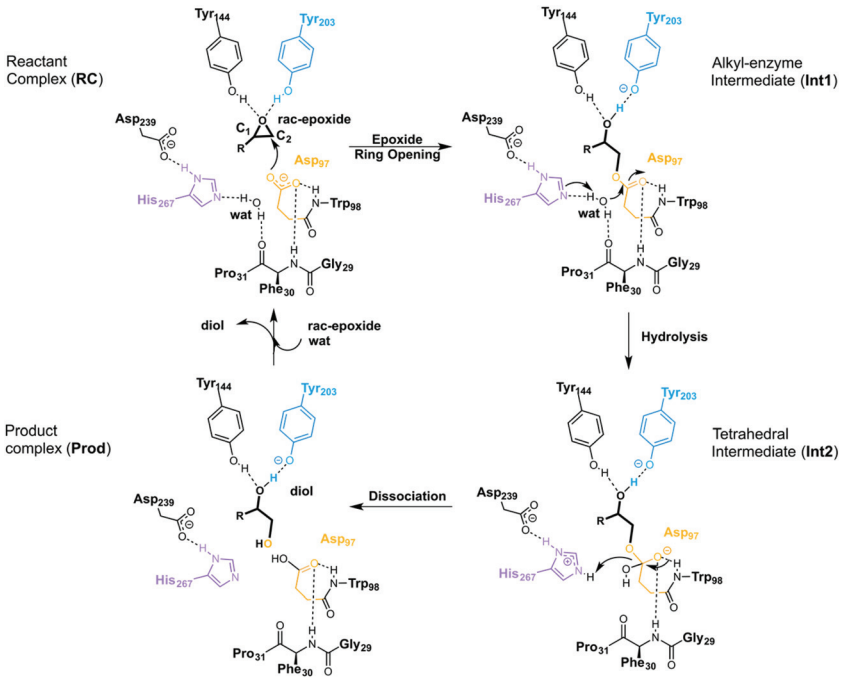

Scheme 2 General reaction mechanism of soluble EH enzymes. BmEH wild-type (PDB: 4NZZ labelling).

enantiomer the attack at C2 is favoured. Both cases lead to the formation of the (*R*)-diol, thus highlighting the enantioconvergent behaviour of StEH1 for the SO substrate. This is in contrast to previous results by Amrein *et al.* obtained for the TSO substrate, for which the reaction was favoured at the C2 position for both enantiomers. For TSO and (*S*)-SO substrates, the hydrolysis step was found to be the selectivity determining,[30,41] whereas for the (*R*)-SO substrate the alkylation step is found to determine the regioselectivity of the process.

It should also be pointed out that Lind and Himo investigated the role of the protonation state of the histidine placed close to the catalytic Asp in the catalytic reaction. Their computed energy profiles suggested that including the doubly protonated His104 has a minor effect on their computed energy barriers. These studies show how despite all mechanistic studies carried out to date, the fine details of the sEHs mechanism still remain incompletely understood.

As most EHs preferentially accept the (*S*)-epoxide enantiomer, the comprehension of how (*R*)-selective BmEH operates, and the main factors that contribute to its selectivity and efficiency is of great interest. In this study, we computationally investigate the origins of the enantio- and regioselectivity in BmEH towards *rac*-SO and its derivative *rac*-*p*-NSO using density functional theory (DFT) calculations within the cluster model framework. We have computed the full reaction profile using a consciously designed quantum CM from the BmEH active site (PDB: 4NZZ) consisting of 195 and 197 atoms for *rac*-SO and *rac*-*p*-NSO, respectively (see Fig. 2 and Computational methods). Our results show that styrene oxide and its *para*-nitro derivative switch the inherent BmEH enantio- and regioselectivity, and demonstrate the minor effect of the nitro group on the enzyme selectivity.

2. Results and discussion

The BmEH enzyme presents different features in comparison with other EHs. The BmEH crystal structure, shown in Fig. 1, revealed that this enzyme has an independent product-release site (called region 3) that is not found in other EHs.[6] The active site tunnel (region 2) connecting the substrate-entrance site (region 1) and the product-release site (region 3) was previously identified by an 80 ns Molecular Dynamics (MD) simulation.[6] BmEH exhibits opposite (*R*)-selectivity in comparison with many other (*S*)-specific EHs, thereby providing an alternative approach to obtain those optically pure (*S*) aromatic epoxides, commonly identified as building blocks of active β-adrenergic agents.[12] Many experimental studies reported on how the structure of the substrate or the presence of substituents on the aromatic ring moiety can switch the inherent selectivity of EHs.[42] The inherent (*R*)-selectivity that BmEH exhibits for phenyl glycidyl ethers (PGE) is switched towards (*S*)-selectivity when the styrene oxide (SO) substrate and its *p*-NO_2 derivative are considered.[12] In order to shed some light on the role of the substrate structure and its substitution pattern, as well as to explore the origins of BmEH selectivity, we performed DFT-D3BJ calculations of both racemic styrene oxide (*rac*-SO) and racemic *para*-nitro styrene oxide (*rac*-*p*-NSO). Based on the X-ray BmEH wild-type structure and our MD simulations on the alkyl intermediate **Int1**, we have devised a truncated cluster model (CM) as done by Himo in

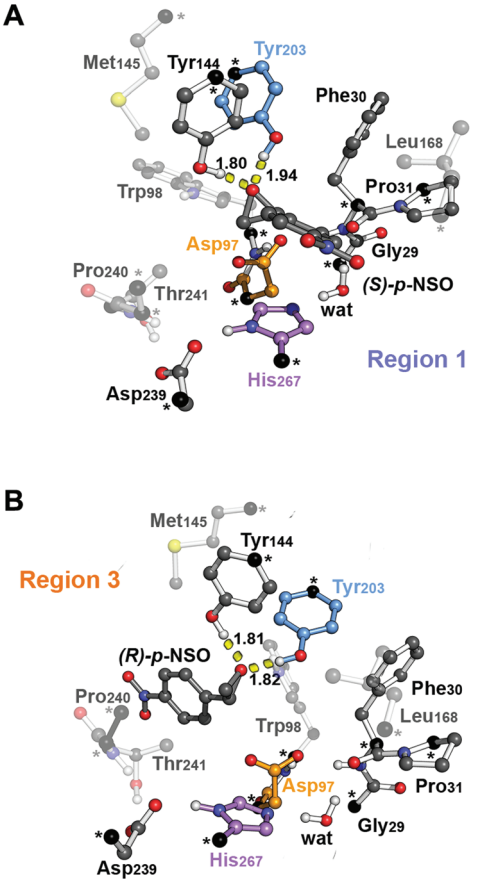

Fig. 2 B3LYP-D3BJ/6-311+g(2d,2p)//B3LYP/6-31g(d,p) optimized geometries of the CM enzyme-structure complex (**RC**) in the active site model with (A) the phenyl substituent of (*S*)-*p*-NSO epoxide pointing towards the catalytic His267 residue (region 1, **RC-S-r1**) and (B) the phenyl substituent of (*R*)-*p*-NSO pointing towards Trp98 (region 3, **RC-R-r3**) (residue labelling as in BmEH). Active site pocket residues are shown as transparent sticks and spheres. Non-polar hydrogen atoms are omitted for clarity. The Asp97 nucleophile, the His267 base and the acid Tyr203 are highlighted in orange, violet, and blue, respectively. Atoms in black spheres and asterisks are kept fixed.

previous studies (see Fig. 2 and Computational methods in the ESI†).[29,43]

To investigate the origins of BmEH selectivity we have computed the EH mechanism described in Scheme 2, considering the first nucleophilic attack either at the epoxide-ring benzylic C1 or the terminal C2 positions for each enantiomer, but also accounting for the two possible substrate orientations regarding the BmEH active site tunnel regions (see Fig. 1 and 2).

Mechanism and selectivity of the BmEH enzyme with the *rac-p*-NSO substrate

The computed reaction energy profiles at the B3LYP-D3BJ/6-311+g(2d,2p)//B3LYP/6-31g(d,p) level of theory for all possible outcomes of *rac-p*-NSO BmEH hydrolysis are represented in Fig. 3. The DFT optimized structures of intermediates (**Int**), products (**Prod**), and transition states (**TS**) for the attack at the benzylic position (C1) of (*S*)-*p*-NSO oriented towards region 1 are shown in Fig. 4.

From our computed energy profiles, small energy differences exist between both region 1 and 3 orientations of the substrate (*ca.* 0.6 kcal mol^{-1}) in the enzyme–substrate complexes (**RC**) for the (*S*)-enantiomer, whereas a difference of *ca.* 3.0 kcal mol^{-1} is found for (*R*)-*p*-NSO **RC**. As shown in Fig. 2, in the DFT optimized **RC** geometries, the epoxide ring forms hydrogen bonds with both Tyr144 and Tyr203 residues, and C1 and C2 carbons are well pre-organized for the subsequent Asp97 nucleophilic attack. The carboxylate side-chain of Asp97 is well positioned for the catalysis thanks to hydrogen bond interactions with the amide backbone groups of Asp97–Trp98 and Gly29–Phe30. The ion-pair charge relay system consisting of Asp239–His267 residues properly interacts for assisting the water molecule activation. In addition, the position of the nucleophilic water is maintained fixed at the active site by hydrogen bonds to the general base His267 and to the backbone carbonyl group of Phe30–Pro31 residues.

The first step of the reaction mechanism after the enzyme–substrate complex (**RC-S-r1**) consists of the nucleophilic attack of Asp97 either at the most substituted carbon C1 (inverting its configuration) or at the less sterically hindered C2 of the epoxide ring to form an ester intermediate (retaining configuration, **Int1-S-C1-r1**, see Fig. 4B). The optimized TS for the Asp97 nucleophilic attack at the C1 position in (*S*)-*p*-NSO (**TS1-S-C1-r1**) exhibits a 2.25 Å distance between the O-Asp97 side-chain and the epoxide C1 atom. The distance between the epoxide oxygen and C1 atom is elongated up to 1.88 Å (see Fig. 4A), corresponding to an S_N2-like concerted TS. The O–H distance of Tyr203 is slightly elongated (from 0.98 Å to 1.00 Å) in the alkylation TS, and the proton is completely transferred from Tyr203 to the epoxide O atom in the optimized covalently-bound enzyme intermediate **Int1-S-C1-r1** (see Fig. 4B). The associated reaction barrier for **TS1-S-C1-r1** is 1.8 kcal mol^{-1} relative to the reactant complex (**RC-S-r1**), and is 0.3 kcal mol^{-1} lower in energy than **TS1-S-C2-r1** corresponding to the attack at the less hindered C2 position (see Fig. 3A). These results show that the intrinsic preference of the enzyme is to perform the nucleophilic attack at the C1 position of (*S*)-*p*-NSO. The resulting **Int1-S-C1-r1** is stabilized by 18.4 kcal mol^{-1}. Regarding the (*R*)-*p*-NSO energy profile diagram, the lowest alkylation TS (**TS1-R-C1-r3**) has an energy of 5.5 kcal mol^{-1} relative to **RC-R-r1** (see Fig. 3B). Comparing both enantiomers, the lowest alkylation transition state (**TS1**) for each enantiomer differs by *ca.* 3.7 kcal mol^{-1}. Note that the orientation of the phenyl ring of the epoxide is different for each case (see Fig. 4A and Fig. S2†). For the (*S*)-enantiomer, the phenyl substituent points towards His267, *i.e.* here called region 1, whereas the lowest alkylation energy barrier for the (*R*)-enantiomer is found when in the **TS1** the phenyl substituent points towards Trp98 *i.e.* region 3 (see Fig. 2B). The analysis of both TS geometries indicates that the additional stabilization of **TS1-S-C1-r1** might be due to the π-stacking interaction between (*S*)-*p*-NSO and the His267 residue, which is not possible in the **R-C1-r3** case (see Fig. 4A and 5). Thus, at this first

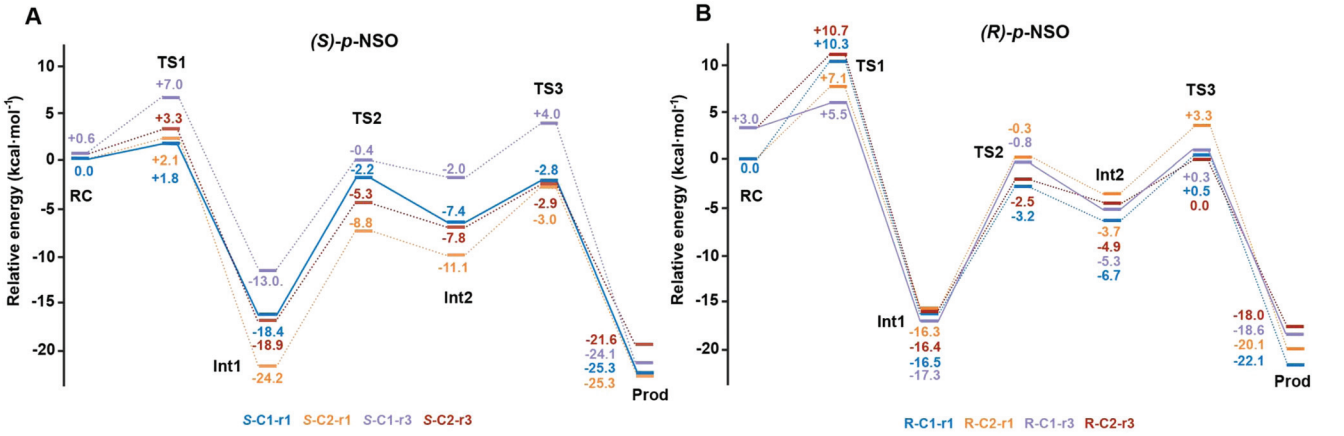

Fig. 3 Energy profiles at the B3LYP-D3BJ/6-311+g(2d,2p)//B3LYP/6-31g(d,p) level of theory for all possible BmEH-mediated epoxide *rac*-*p*-NSO hydrolysis outcomes. All energies are in kcal mol^{-1} and referenced to the lowest energy **RC** for each enantiomer, **RC-S-r1** and **RC-R-r1**, respectively. The kinetically favoured attack for each enantiomer is shown as solid lines (**S-C1-r1** and **R-C1-r3**), the other possible pathways are shown as dashed lines.

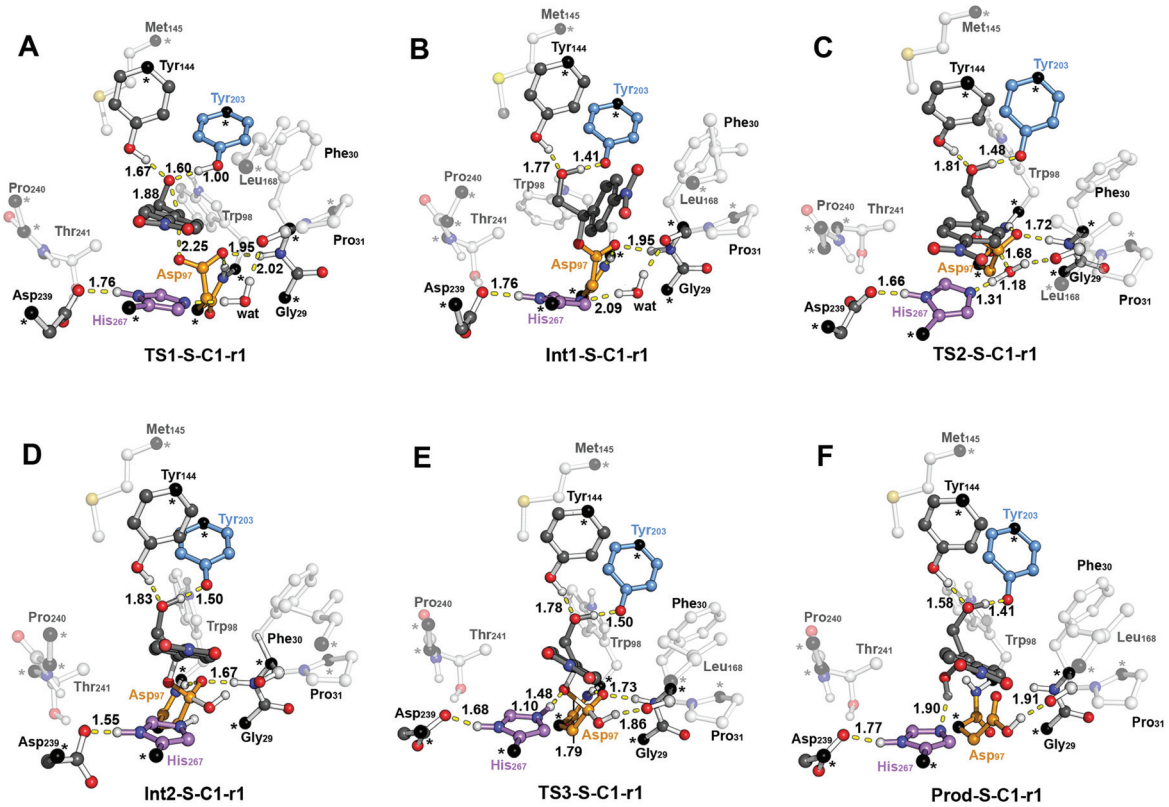

Fig. 4 B3LYP-D3BJ/6-311+g(2d,2p)//B3LYP/6-31g(d,p) optimized geometries corresponding to the different steps of the BmEH mechanism of action for the (*S*)-*p*-NSO substrate oriented towards region 1 for the attack at the benzylic position (C1): (A) epoxide ring opening (**TS1-S-C1-r1**), (B) alkyl-enzyme intermediate (**Int1-S-C1-r1**), (C) hydrolysis of the alkyl-enzyme intermediate (**TS2-S-C1-r1**), (D) tetrahedral intermediate (**Int2-S-C1-r1**), (E) dissociation of tetrahedral (**TS3-S-C1-r1**) and (F) product complex (**Prod-S-C1-r1**). All distances are in Å. Active site pocket residues are shown as transparent sticks and spheres and non-polar hydrogen atoms are omitted for clarity. Atoms in black spheres and asterisks are kept fixed.

stage of the BmEH mechanism, our computed energy profiles indicate that the epoxide ring opening of (*S*)-*p*-NSO is more favoured than the (*R*)-enantiomer.

The next step in the reaction mechanism includes the nucleophilic attack by a water molecule (**wat**) to hydrolyse the previously formed ester bond, and the dissociation of the tetra-

hedral intermediate (**Int2**) generated at this half-hydrolytic reaction to yield the vicinal diol (**Prod**, see Scheme 2). In the DFT optimized **TS2-S-C1-r1**, the neutral His267 residue acts as a general base to activate the water molecule that attacks Asp97 generating the **Int2-S-C1-r1** intermediate, as shown in Fig. 4C. The activation of the water molecule is possible because at **TS2-S-C1-r1** the Asp239–His267 distance has been substantially shortened, allowing the stabilization of the protonated state of His267. Likewise, the observed distances in **Int2-S-C1-r1** between the carbonyl oxygen atom of Asp97 and the amide bonds of Asp97–Trp98 and Gly29–Phe30 in the oxyanion hole indicate that the negative charge that arises at this stage is well stabilized (shorter distances of *ca.* 1.67 Å, see Fig. 4D). All these observed networks of interactions allow **TS2** stabilization, thereby making it possible to overcome the computed **Int1** → **TS2** barriers of 16.2 kcal mol^{-1}. Similar energy barriers were found for the most favoured (*R*)-enantiomer attack (**TS2-R-C1-r3**, $\Delta E^{\ddagger}$ = 16.5 kcal mol^{-1}), in which the covalent enzyme intermediate **Int1-R-C1-r3** was found to be stabilized by 17.3 kcal mol^{-1}.

To generate the final diol product, a final step is needed in which the C–O bond between the epoxide substrate and Asp97 is cleaved, followed by subsequent protonation (see Scheme 2). The corresponding transition state **TS3-S-C1-r1** ($\Delta E^{\ddagger}$ = 4.6 kcal mol^{-1} with respect to **Int2**) presents elongated C–O distances (*ca.* 1.79 Å), and the protonated His267 interacts with the (*S*)-*p*-NSO substrate delivering a proton for 1,2-diol formation (*ca.* 1.48 Å) as shown in Fig. 4E. Therefore, the catalytic His267 found to be important in the previous step for catalysing the hydrolysis acting as a general base has also a critical role at this final step for 1,2-diol generation. Note that this C–O bond breaking generates a diol product in which one of the oxygen atoms comes from the nucleophilic Asp97 residue (see Scheme 2). The activation barrier for the dissociative transition state **TS3** for the (*R*)-enantiomer (**TS3-R-C1-r3**) is 5.6 kcal mol^{-1} with respect to **Int2**. As previously mentioned for the alkylation transition state (**TS1**), since for (*R*)-*p*-NSO the phenyl ring points towards region 3, this might lead to a less stabilized **TS3** due to the lack of π-stacking interaction with the catalytic His267 residue (see Fig. S3†).

As shown in Fig. 4F, the new hydroxyl group in the product **Prod-S-C1-r1** interacts with Tyr144-O–H (*ca.* 1.58 Å) and the deprotonated Tyr203-O^{-} (*ca.* 1.41 Å). **Prod-S-C1-r1** is −25.3 kcal mol^{-1} more stable than **RC-S-r1**, whereas for the (*R*)-enantiomer **Prod-R-C1-r3** is −18.6 kcal mol^{-1} lower in energy than **RC-R-r1**. In all optimized **Prod** structures, Asp97 is in its protonated state whereas Tyr203 remains deprotonated. Thus, an additional acid–base step is needed, and the binding of a new epoxide and water molecule is required to regenerate the catalytic cycle (see Scheme 2). These steps are difficult to be accurately described with the current methodology.[41] As proposed by Himo in previous studies,[41] the overall energetics of the process can be roughly approximated by computing the free energy of the (*S*)-epoxide + water → (*R*)-1,2-diol reaction, which is exergonic by 8 kcal mol^{-1}. This large energetic span between **Prod-S-C1-r1** and **RC** (−8 + 25.3 = 17.3 kcal mol^{-1}) should be added to the alkylation activation barrier of the next cycle, thus yielding an approximated barrier of *ca.* 19 kcal mol^{-1} for (*S*)-*p*-NSO. This estimation indicates that both alkylation and hydrolysis steps present similar barriers. Due to the large inaccuracies associated with the estimation of the **Prod** → **React** process, we focus our analysis on the computed reaction pathway displayed in Fig. 3, which shows that alkylation is selectivity-determining, whereas hydrolysis is rate-determining. Thus, to directly compare the reactivities of (*S*) and (*R*) substrates, we evaluate the activation barriers for the rate-determining hydrolysis step in the pathways that have the lowest alkylation barriers (**TS1**) for each enantiomer, *i.e.* **S-C1-r1** and **R-C1-r3**, respectively.

Overall our computed reaction pathways indicate that the lowest energy intermediate corresponds to **Int1**, and the rate-determining transition state is **TS2** for **S-C1-r1** and **TS3** for **R-C1-r3** both corresponding to the dissociation of the covalently bound enzyme intermediate (**Int1** in Scheme 2). The computed barriers are 16.2 kcal mol^{-1} for (*S*)-*p*-NSO (**S-C1-r1** in Fig. 3A), whereas 17.6 kcal mol^{-1} for (*R*)-*p*-NSO (**R-C1-r3** in Fig. 3B). Therefore, the hydrolysis of the (*S*)-enantiomer is kinetically favoured by *ca.* 1.4 kcal mol^{-1}, which is in agreement with experimental observations for BmEH.[12] It should also be noted that our computed activation barriers are in line with the experimental rate constants of 3–10 s^{-1} at 30 °C (*ca.* 16–17 kcal mol^{-1}) for the related StEH1 enzyme.[44,45]

Substituent effect on the BmEH selectivity

Using DFT-D3BJ calculations we also examined the hydrolysis of the racemic styrene oxide (*rac*-SO) substrate to further explore how the substrate structure and its substitution pattern affect BmEH selectivity. To this aim, we also considered all possible outcomes for *rac*-SO, *i.e.* the nucleophilic attack either at benzylic C1 or terminal carbon C2 for each enantiomer oriented towards region 1 or 3 as described above (see Fig. 1 and Fig. S4†).

The computed energy profiles for the *rac*-SO substrate follow a similar trend to those discussed in the previous section for its *para*-nitro derivative substrate *rac-p*-NSO (see Fig. 3 and Fig. S4†). As observed for *rac-p*-NSO energy profiles, the most favoured outcome for (*S*)-SO epoxide comes from the nucleophilic attack at the benzylic position (C1) when the phenyl moiety of the substrate is oriented towards His267 ($\Delta E^{\ddagger}$ = 4.0 kcal mol^{-1} with respect to **RC-S-SO-r1**, and $\Delta E^{\ddagger}$ = 15.3 kcal mol^{-1} computed from the lowest energy **Int1**, for **TS3-S-SO-C1-r1**).

For the (*R*)-enantiomer, the kinetically favored attack is found when the phenyl ring is oriented towards region 3. The alkylation barrier of **TS1-R-SO-C1-r3** is 6.6 kcal mol^{-1} regarding the lowest energy **RC** for (*R*)-SO (**RC-R-SO-r1**, see Fig. S4†). The alkylation at position C2 is *ca.* 0.5 kcal mol^{-1} less favorable than the attack at C1 (**TS1-R-SO-C2-r3**). The hydrolysis step of **Int1** is kinetically more favoured at the terminal carbon C2 as the computed activation barriers are *ca.* 19.8 and 17.4 kcal mol^{-1} for **TS3-R-SO-C1-r3** and **TS3-R-SO-C2-r3**,

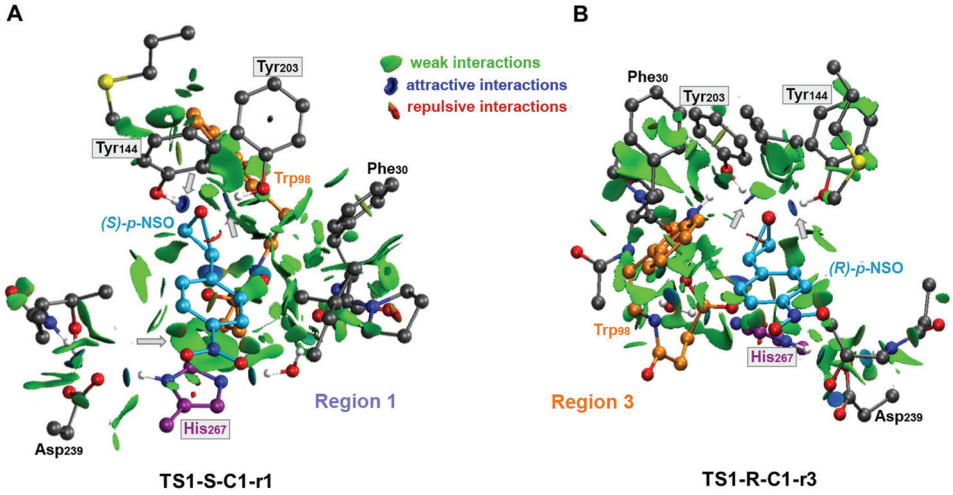

Fig. 5 Non-covalent interaction representation of the lowest energy alkylation transition states (A) **TS1-S-C1-r1** and (B) **TS1-R-C1-r3** for the *rac*-*p*-NSO epoxide ring opening reaction using the NCIplot computational tool.[44,45] NCI surfaces show intermolecular interactions between the epoxide substrate and the active site residues included in the CM model. All residues are represented as balls and sticks and the two possible orientations for each substrate are indicated for each case (region 1, His267 and region 3, Trp98). Only the most important catalytic residues are labelled regarding BmEH (PDB: 4NZZ numbering) and non-polar hydrogen are not shown for clarity. Grey arrows are used to highlight the most important noncovalent interactions. The most important residues are framed.

respectively (computed from the lowest energy intermediate **Int1**).

As observed for *p*-NSO, the activation barriers obtained (shown in Fig. S4†) for (*S*)-SO at C1 are *ca.* 2.6 kcal mol^{-1} lower than those obtained for (*R*)-SO, thus suggesting that the nitro group has a very minor effect on the enantio- and regioselectivity of the process.

Overall our mechanistic studies also indicate that both *rac*-*p*-NSO and *rac*-SO switch the inherent (*R*)-BmEH selectivity observed towards PGE substrates, as described in previous experimental studies. A higher enantioselectivity of BmEH towards *rac*-*p*-NSO ($ee_s \geq 99\%$) than for *rac*-SO ($ee_s = 53\%$) was observed experimentally.[12] The energy differences between our computed activation barriers overestimate the ee for *rac*-SO. However, the relative stabilities of the **RCs** indicate that the binding of (*R*)-epoxides for both *p*-NSO and SO is more favourable than for (*S*), especially in region 1 due to the higher stabilization by non-covalent interactions with the active site residues, including π···π with His267 (see Fig. 5). Our computed energy differences between substrate bound **RCs** ((*R*) *vs.* (*S*)) for *p*-NSO are *ca.* 3.0 kcal mol^{-1}, while it is only 1.4 kcal mol^{-1} for *rac*-SO. Thus, the higher enantioselectivity observed experimentally for *rac*-*p*-NSO can be attributed to the more favourable unproductive binding of (*R*)-*p*-NSO in region 1, as in this region the activation barriers for the alkylation and hydrolysis step are *ca.* 2 kcal mol^{-1} higher than in region 3.

Our calculations show that in the BmEH catalysed hydration of *rac*-*p*-NSO and *rac*-SO, **TS3** energies are in general lower than **TS1**. This is in contrast to *rac*-SO hydrolysis by StEH1,[41] where Himo and coworkers found that the hydrolysis step (**TS3**) is generally higher in energy than **TS1**. Although the energy differences are rather small (*ca.* ±3 kcal mol^{-1}), our results show that the shape and conformation of the active site pocket, as well as the substrate orientation will modulate the selectivity-determining step, *i.e.* the alkylation (**TS1**) or the hydrolysis (**TS3**).

3. Conclusions

Our DFT-D3BJ calculations within the CM framework indicate that the substrate structure switches the usual BmEH (*R*)-selectivity towards (*S*) when racemic styrene oxide (*rac*-SO) and racemic *para*-nitro styrene oxide (*rac*-*p*-NSO) are considered. The computed energy profiles for the different substrates and enantiomers suggest that the first alkylation step (**TS1**) is responsible for the regioselectivity of the process, while the hydrolysis half reaction is the rate-limiting step. In both *rac*-SO and *rac*-*p*-NSO the (*S*)-enantiomer is preferentially attacked at the benzylic position (C1) when the phenyl ring moiety points towards region 1 (*i.e.* the substrate entrance). This orientation maximizes the π···π interactions between the substrate (both SO, and *p*-NSO) and the active site residues, in particular His267. Therefore, the catalytically competent poses of the (*S*)-enantiomer of the aromatic SO and *p*-NSO substrates are found in region 1. The least reactive (*R*)-epoxide has a preferential binding for region 1, however in this region the activation barriers are substantially higher as compared to those in region 3. This work demonstrates that the enantiopreference of BmEH towards aromatic epoxides can be directly assessed by the combination of DFT-D3BJ and the analysis of non-covalent interactions, and provides an alternative strategy for the engineering of EHs towards the resolution of synthetically useful epoxides.

Computational methods

Full geometry optimizations were performed with the hybrid DFT B3LYP functional[46,47] and the 6-31G(d) basis set[48,49] using Gaussian 09,[50] a widely accepted level of theory for studying mechanisms of organic reactions.[51,52] The effects of the active site environment of the protein were implicitly included in all calculations using the Conductor-like Polarizable Continuum Model (CPCM)[53,54] with diethyl ether as the solvent ($\varepsilon = 4$). The transition states (TS) were located by using a Bofill update TS search on a reduced potential energy surface.[55] Analytical frequency calculations were performed at the same level of theory as the geometry optimizations to obtain the zero point energies (ZPE). The nature of the stationary points was determined in each case according to the Hessian matrix eigenvalues. We have also checked that imaginary frequencies exhibit the expected motion, while transition states have also been verified by intrinsic reaction coordinate (IRC) calculations. More accurate energies were obtained by single-point calculations including the DFT hybrid B3LYP-D3BJ dispersion correction with the larger 6-311+G(2d,2p) basis set. All energies are ZPE-corrected.

Active site model. The quantum chemical model used has been devised based on the most populated cluster from a 1000 ns MD simulation on the alkyl-enzyme intermediate (**Int1**, see full details in the ESI†). The starting structure was obtained from the X-ray crystal structure of wild-type BmEH from the PDB structure: 4NZZ. The cluster model consists of: an Asp239–His267–Asp97 catalytic triad, two active Tyr144 and Tyr203 residues, a nucleophilic water molecule and two hydrogen bonded amide bonds (Gly29–Phe30 and Phe30–Pro31 from the oxyanion motif HGFP). In addition, Trp98, Leu168, Met145, Thr241, and Pro240 residues were also included to appropriately describe the shape of the active site cavity of the $BmEH_{4NZZ}$ enzyme. All amino acids were truncated at the α- or β-carbon, except for the tyrosines, which are modelled as phenols and for Pro240, in which only the α- and its side-chain carbon attached are included to properly simulate the conformational rigidity of proline. Atoms in black (and highlighted with asterisks) shown in Fig. 2 are kept fixed to their initial Cartesian coordinates during the optimizations. Hydrogen atoms were included manually based on either the literature or the $BmEH_{4NZZ}$ active site rearrangement, resulting in two aspartate Asp97 and Asp239 active site residues modelled as in the negatively charged state, whereas His267 was modelled in the neutral form, obtaining a quantum model with an overall charge of −2 (see Fig. 2).

The epoxide substrates used to model the mechanisms were the racemic styrene oxide (*rac*-SO) and its racemic *para* nitro-substituted derivative (*rac-p*-NSO, cluster models of 195 and 197 atoms, respectively). To explore the origins of the enantio- and regioselectivity of BmEH and the effect of the presence of the NO_2 group, all plausible reaction mechanisms should be considered. Thus, a total of 16 reaction pathways need to be computed to take into account that the EH hydrolysis of *rac*-epoxides can take place *via* an attack on either carbon atom of each enantiomer, and also two possible binding orientations of the substrate on the basis of the proposed BmEH active site tunnel.[6] The two possible binding poses arise from the orientation of the phenyl moiety of the substrate towards either region 1 (**r1**) placing the phenyl moiety close to His267, or region 3 (**r3**) when it points towards Trp98 (see Fig. 1 and 2).

Conflicts of interest

There are no conflicts to declare.

Acknowledgements

E. S.-H. thanks the Generalitat de Catalunya for a PhD fellowship (2017-FI-B-00118), M. G.-B. is grateful to the Ramón Areces Foundation for a Postdoctoral Fellowship. S. O. thanks the Spanish MINECO CTQ2014-59212-P, Ramón y Cajal contract (RYC-2014-16846), the European Community for CIG project (PCIG14-GA-2013-630978), and the funding from the European Research Council (ERC) under the European Union's Horizon 2020 research and innovation programme (ERC-2015-StG-679001). We are grateful for the computer resources, technical expertise, and assistance provided by the Barcelona Supercomputing Center – Centro Nacional de Supercomputacion.

Notes and references

1 A. Archelas and R. Furstoss, *Curr. Opin. Chem. Biol.*, 2001, **5**, 112–119.
2 E. J. de Vries and D. B. Janssen, *Curr. Opin. Biotechnol.*, 2003, **14**, 414–420.
3 A. Archelas and R. Furstoss, *Trends Biotechnol.*, 1998, **16**, 108–116.
4 P. Besse and H. Veschambre, *Tetrahedron*, 1994, **50**, 8885–8927.
5 K. Michael, A. Alain and W. Roland, *Curr. Org. Chem.*, 2012, **16**, 451–482.
6 X.-D. Kong, S. Yuan, L. Li, S. Chen, J.-H. Xu and J. Zhou, *Proc. Natl. Acad. Sci. U. S. A.*, 2014, **111**, 15717–15722.
7 F. E. Held, S. Wei, K. Eder and S. B. Tsogoeva, *RSC Adv.*, 2014, **4**, 32796–32801.
8 A. Schmid, K. Hofstetter, H. J. Feiten, F. Hollmann and B. Witholt, *Adv. Synth. Catal.*, 2001, **343**, 732–737.
9 P. Berglund, *ChemBioChem*, 2006, **7**, 1280–1280.
10 M. Smit and M. Labuschagné, *Curr. Org. Chem.*, 2006, **10**, 1145–1161.
11 B. Van Loo, J. Kingma, M. Arand, M. G. Wubbolts and D. B. Janssen, *Appl. Environ. Microbiol.*, 2006, **72**, 2905–2917.
12 J. Zhao, Y.-Y. Chu, A.-T. Li, X. Ju, X.-D. Kong, J. Pan, Y. Tang and J.-H. Xu, *Adv. Synth. Catal.*, 2011, **353**, 1510–1518.

13 Y.-F. Tang, J.-H. Xu, Q. Ye and B. Schulze, *J. Mol. Catal. B: Enzym.*, 2001, **13**, 61–68.
14 P.-F. Gong and J.-H. Xu, *Enzyme Microb. Technol.*, 2005, **36**, 252–257.
15 Y. Xu, J.-H. Xu, J. Pan and Y.-F. Tang, *Biotechnol. Lett.*, 2004, **26**, 1217–1221.
16 M. T. Reetz, C. Torre, A. Eipper, R. Lohmer, M. Hermes, B. Brunner, A. Maichele, M. Bocola, M. Arand and A. Cronin, *Org. Lett.*, 2004, **6**, 177–180.
17 M. T. Reetz, L. W. Wang and M. Bocola, *Angew. Chem., Int. Ed.*, 2006, **118**, 1258–1263.
18 P. Moussou, A. Archelas, J. Baratti and R. Furstoss, *J. Org. Chem.*, 1998, **63**, 3532–3537.
19 S. Barth, M. Fischer, R. D. Schmid and J. Pleiss, *Proteins: Struct., Funct., Bioinf.*, 2004, **55**, 846–855.
20 M. Nardini and B. W. Dijkstra, *Curr. Opin. Struct. Biol.*, 1999, **9**, 732–737.
21 D. Lindberg, S. Ahmad and M. Widersten, *Arch. Biochem. Biophys.*, 2010, **495**, 165–173.
22 R. N. Armstrong and C. S. Cassidy, *Drug Metab. Rev.*, 2000, **32**, 327–338.
23 K. H. Hopmann and F. Himo, *J. Phys. Chem. B*, 2006, **110**, 21299–21310.
24 R. N. Patel, *Green Biocatalysis*, John Wiley & Sons, 2016.
25 W. J. Choi, *Appl. Microbiol. Biotechnol.*, 2009, **84**, 239–247.
26 P. Bauer, A. J. Carlsson, B. A. Amrein, D. Dobritzsch, M. Widersten and S. C. L. Kamerlin, *Org. Biomol. Chem.*, 2016, **14**, 5639–5651.
27 D. Lindberg, A. Gogoll and M. Widersten, *FEBS J.*, 2008, **275**, 6309–6320.
28 E. Y. Lee and M. L. Shuler, *Biotechnol. Bioeng.*, 2007, **98**, 318–327.
29 K. H. Hopmann and F. Himo, *Chem. – Eur. J.*, 2006, **12**, 6898–6909.
30 B. A. Amrein, P. Bauer, F. Duarte, A. J. Carlsson, A. Naworyta, S. L. Mowbray, M. Widersten and S. C. L. Kamerlin, *ACS Catal.*, 2015, **5**, 5702–5713.
31 K. H. Hopmann and F. Himo, *J. Phys. Chem. B*, 2006, **110**, 21299–21310.
32 B. Schiott and T. C. Bruice, *J. Am. Chem. Soc.*, 2002, **124**, 14558–14570.
33 M. T. Reetz, M. Bocola, L.-W. Wang, J. Sanchis, A. Cronin, M. Arand, J. Zou, A. Archelas, A.-L. Bottalla, A. Naworyta and S. L. Mowbray, *J. Am. Chem. Soc.*, 2009, **131**, 7334–7343.
34 R. N. Armstrong, *Drug Metab. Rev.*, 1999, **31**, 71–86.
35 G. M. Lacourciere and R. N. Armstrong, *J. Am. Chem. Soc.*, 1993, **115**, 10466–10467.
36 C. Morisseau and B. D. Hammock, *Annu. Rev. Pharmacol. Toxicol.*, 2005, **45**, 311–333.
37 A. Romero-Rivera, M. Garcia-Borràs and S. Osuna, *Chem. Commun.*, 2017, **53**, 284–297.
38 K. Hotta, X. Chen, R. S. Paton, A. Minami, H. Li, K. Swaminathan, I. I. Mathews, K. Watanabe, H. Oikawa, K. N. Houk and C.-Y. Kim, *Nature*, 2012, **483**, 355–358.
39 Y. Zou, M. Garcia-Borràs, M. C. Tang, Y. Hirayama, D. H. Li, L. Li, K. Watanabe, K. N. Houk and Y. Tang, *Nat. Chem. Biol.*, 2017, **13**, 325–332.
40 L. T. Elfström and M. Widersten, *Biochem. J.*, 2005, **390**, 633–640.
41 M. E. S. Lind and F. Himo, *ACS Catal.*, 2016, 8145–8155.
42 P. Moussou, A. Archelas, J. Baratti and R. Furstoss, *Tetrahedron: Asymmetry*, 1998, **9**, 1539–1547.
43 K. H. Hopmann, B. M. Hallberg and F. Himo, *J. Am. Chem. Soc.*, 2005, **127**, 14339–14347.
44 J. Contreras-García, E. R. Johnson, S. Keinan, R. Chaudret, J.-P. Piquemal, D. N. Beratan and W. Yang, *J. Chem. Theory Comput.*, 2011, **7**, 625–632.
45 E. R. Johnson, S. Keinan, P. Mori-Sánchez, J. Contreras-García, A. J. Cohen and W. Yang, *J. Am. Chem. Soc.*, 2010, **132**, 6498–6506.
46 C. Lee, W. Yang and R. G. Parr, *Phys. Rev. B: Condens. Matter*, 1988, **37**, 785–789.
47 A. D. Becke, *J. Chem. Phys.*, 1993, **98**, 5648–5652.
48 P. C. Hariharan and J. A. Pople, *Theor. Chim. Acta*, 1973, **28**, 213–222.
49 W. J. Hehre, R. Ditchfield and J. A. Pople, *J. Chem. Phys.*, 1972, **56**, 2257–2261.
50 M. J. Frisch, G. W. Trucks, H. B. Schlegel, G. E. Scuseria, M. A. Robb, J. R. Cheeseman, G. Scalmani, V. Barone, B. Mennucci, G. A. Petersson, H. Nakatsuji, M. Caricato, X. Li, H. P. Hratchian, A. F. Izmaylov, J. Bloino, G. Zheng, J. L. Sonnenberg, M. Hada, M. Ehara, K. Toyota, R. Fukuda, J. Hasegawa, M. Ishida, T. Nakajima, Y. Honda, O. Kitao, H. Nakai, T. Vreven, J. A. Montgomery, Jr., J. E. Peralta, F. Ogliaro, M. Bearpark, J. J. Heyd, E. Brothers, K. N. Kudin, V. N. Staroverov, R. Kobayashi, J. Normand, K. Raghavachari, A. Rendell, J. C. Burant, S. S. Iyengar, J. Tomasi, M. Cossi, N. Rega, J. M. Millam, M. Klene, J. E. Knox, J. B. Cross, V. Bakken, C. Adamo, J. Jaramillo, R. Gomperts, R. E. Stratmann, O. Yazyev, A. J. Austin, R. Cammi, C. Pomelli, J. W. Ochterski, R. L. Martin, K. Morokuma, V. G. Zakrzewski, G. A. Voth, P. Salvador, J. J. Dannenberg, S. Dapprich, A. D. Daniels, Ö. Farkas, J. B. Foresman, J. V. Ortiz, J. Cioslowski and D. J. Fox, *Gaussian 09, Revision D.01*, Gaussian, Inc., Wallingford CT, 2013.
51 G. Kiss, N. Celebi-Oelcuem, R. Moretti, D. Baker and K. N. Houk, *Angew. Chem., Int. Ed.*, 2013, **52**, 5700–5725.
52 F. Himo, *Theor. Chem. Acc.*, 2006, **116**, 232–240.
53 V. Barone and M. Cossi, *J. Phys. Chem. A*, 1998, **102**, 1995–2001.
54 V. Barone, M. Cossi and J. Tomasi, *J. Comput. Chem.*, 1998, **19**, 404–417.
55 S. K. Burger and P. W. Ayers, *J. Chem. Phys.*, 2010, **132**, 234110.